International Journal of Remote Sensing

ISSN: 0143-1161 (Print) 1366-5901 (Online) Journal homepage: http://www.tandfonline.com/loi/tres20

Extracting buildings from and regularizing boundaries in airborne lidar data using connected operators

Zongze Zhao, Yansong Duan, Yongjun Zhang & Rujun Cao

To cite this article: Zongze Zhao, Yansong Duan, Yongjun Zhang & Rujun Cao (2016) Extracting buildings from and regularizing boundaries in airborne lidar data using connected operators, International Journal of Remote Sensing, 37:4, 889-912, DOI: 10.1080/01431161.2015.1137647

To link to this article: http://dx.doi.org/10.1080/01431161.2015.1137647

INTERNATIONAL JOURNAL OF REMOTE SENSING, 2016
VOL. 37, NO. 4, 889–912
http://dx.doi.org/10.1080/01431161.2015.1137647

Taylor & Francis
Taylor & Francis Group

Extracting buildings from and regularizing boundaries in airborne lidar data using connected operators

Zongze Zhao, Yansong Duan, Yongjun Zhang and Rujun Cao

School of Remote Sensing and Information Engineering, Wuhan University, Wuhan, China

ABSTRACT

The location of building boundary is a crucial prerequisite for geographical condition monitoring, urban management, and building reconstruction. This paper presents a framework that employs a series of algorithms to automatically extract building footprints from airborne (light detection and ranging (lidar)) data and image. Connected operators are utilized to extract building regions from lidar data, which would not produce new contours nor change their position and have very good contour-preservation properties. First, the building candidate regions are separated from lidar-derived digital surface model (DSM) based on a new method proposed within this paper using connected operators, and trees are removed based on the normalized difference vegetation index (NDVI) value of image. Then, building boundaries are identified and building boundary lines are traced by 'sleeve' line simplification method. Finally, the principal directions of buildings are used to regularize the directions of building boundary lines. International Society for Photogrammetry and Remote Sensing (ISPRS) data sets in Vaihingen whose point spacing is about 0.4 m from urbanized areas were employed to test the proposed framework, and three test areas were selected. A quantitative analysis showed that the method proposed within this paper was effective and the average offset values of simple and complex building boundaries were 0.2–0.4 m and 0.3–0.6 m, respectively.

ARTICLE HISTORY
Received 8 February 2015
Accepted 20 December 2015

1. Introduction

Airborne light detection and ranging (lidar) technology provides georeferenced 3D dense point measurements over reflective surfaces on the ground (Baltsavias 1999; Wehr and Lohr 1999; Sampath and Shan 2007; Zhang and Shen 2013). Usually, as a premise for many building extraction approaches, the ground points need to be separated from non-ground points, for which a number of filtering methods have been developed. For the moment, the main filtering methods include morphological filtering (Kilian, Haala, and Englich 1996; Zhang et al. 2003; Chen et al. 2007), triangulated irregular network (TIN) filtering (Axelsson 2000), and slope-based filtering (Vosselman 2000).

Currently, numerous methods have been developed to extract building areas from lidar data. Morgan and Tempfli (2000) utilized morphological filtering to distinguish

CONTACT Yongjun Zhang zhangyj@whu.edu.cn

ground and non-ground points, and applied Laplacian and Sobel operators to height surfaces to distinguish between building and tree measurements. Kwak and Habib (2014), and Shan and Sampath (2008) managed to separate ground, building, and tree regions using region growing algorithms. Zhang, Yan, and Chen (2006) employed morphological filtering to separate ground and non-ground regions, and separated building and tree regions using a region growing method. Rottensteiner and Jansa (2002) used the difference between digital surface model (DSM) and digital terrain model to determine the building areas. Sohn and Dowman (2007) differentiated on-terrain and off-terrain features according to recursive terrain fragmentation filtering and high-rise features were separated from off-terrain features by a pre-defined threshold. Chen et al. (2014) detected and reconstructed building roofs from airborne lidar data using a multi-scale grid method. Mongus, Lukač, and Žalik (2014) estimated the geometric attributes of the contained features by mapping characteristic values from differential morphological profiles (DMPs), while their surface and regional attributes were additionally considered for building detection. Chen et al. (2012) employed progressive morphological filter to separate ground and non-ground points and separated building points from vegetation points by a plane-fitting technique. Niemeyer, Rottensteiner, and Soergel (2014) addressed the task of the contextual classification of an airborne lidar point cloud and detected building objects based on the classified point cloud. For a comprehensive literature review, readers may refer to Rottensteiner et al. (2014) who presented several techniques for extracting urban objects from International Society for Photogrammetry and Remote Sensing (ISPRS) benchmarking data.

Connected operators are applied to building extraction from lidar data in this paper. Since connected operators would not produce new contours nor change their position, they have very good contour-preservation properties and are capable of both low-level filtering and high-level object recognition (Salembier and Wilkinson 2009). For this reason, connected operators can be utilized to the operation of lidar data availably (Mongus and Žalik 2014). Besides, max-tree structure, attribute-space connectivity, and area-based filtering criterion are introduced to extract building regions straightforwardly and effectively.

Building boundary determination is a crucial and difficult step in the building reconstruction task (Rottensteiner and Briese 2002). Morgan and Habib (2002) used a TIN model to determine the building boundary from lidar data. Sampath and Shan (2007) extracted building boundaries using a modified convex hull approach. After identifying building boundaries, a raw footprint polygon will consist of some boundary lines. However, the raw footprint is often rough because of the irregularly spaced lidar measurements. It is difficult to acquire an accurate footprint from an irregular and complex polygon. Sampath and Shan (2007) used the least squares model to regularize the boundary lines. However, this assumption is not strict and cannot be applied to buildings whose edges are not perpendicular to the dominant directions (Zhang, Yan, and Chen 2006). Zhang, Yan, and Chen (2006) have proposed a new method to estimate the dominant directions of a building footprint based on weighted line-segment lengths. Our primary contributions in this paper are listed as follows.

- Connected operators are utilized to extract building regions from lidar data, which would not produce new contours nor change their position and have very good contour-preservation properties.
- Max-tree structure, attribute-space connectivity, and area-based filtering criterion are introduced in the process of connected filter to ensure that building regions are discriminated accurately and effectively from lidar data.

In this paper, three steps are involved in building extraction and regularization from lidar data: (1) extracting building regions from the raw lidar data; (2) utilizing the 'sleeve' method to determine the boundary line segments of buildings; and (3) determining the main directions of buildings, regularizing the boundary line segments of buildings based on the main directions.

2. Connected operators

Connected operators (Salembier and Serra 1995; Heijmans 1999) are the efficient image processing tools set in the framework of mathematical morphology. They have been successfully applied to biomedical imaging (Dufour et al. 2013), astronomy (Berger et al. 2007; Perret et al. 2010), remote sensing (Kurtz et al. 2012; Cavallaro et al. 2015), and document analysis (Naegel and Wendling 2010). Connected operators focus on the notion of connection that explains how pixels are grouped together to achieve objects called connected components. They cannot create or shift but only delete connected components. The extension to grey-scale images is realized through threshold superposition, which can be effectively represented by a tree structure naturally leading to the hierarchical representation of image.

2.1. *Connectivity classes*

Binary image X is considered to be the subsets of some universal set V (usually Z^2). Let P (V) be the set of all subsets of V. Connectivity in V can be defined using connectivity classes (Serra 1998; Braga-Neto and Goutsias 2002).

Definition 1. Let V be an arbitrary nonempty set. A connectivity class or connection $C \subseteq P(V)$ is a set of sets that satisfies the following.

1. $\emptyset \in C$ and for all $x \in V, \{x\} \in C$.
2. For any $\{C_i\} \subseteq C, \cap_i C_i \neq \emptyset \Rightarrow \cup_i C_i \in C$.

Any member of C is said to be connected. The definition means that both the empty set and the singleton set ($\{x\}$) are connected, and any union of sets C_i in C which have a nonempty intersection is connected. The members of C are called connected sets and correspond to subsets of V.

2.2. *Attribute filters*

Through definition 1, we know that any binary image X can be taken as a collection of connected components. Connected filters are considered as filters that preserve only

those components that satisfy the given criteria in a binary image. The criteria are based on one or more of the component's attributes (e.g. area or perimeter). The notion of a connected filter may be formalized as follows.

$$\Psi_\Lambda(X) = \bigcup_{C_i \in C} \Gamma_\Lambda(C_i). \tag{1}$$

The subscript 'Λ' denotes a given criterion, and Γ_Λ an operator. For a connected component $C_i \in C$, Γ_Λ returns C_i if $\Lambda(C_i)$ is true and null otherwise. The connected filter Ψ_Λ is anti-extensive ($\Psi_\Lambda(X) \subseteq X$) and idempotent ($\Psi_\Lambda(\Psi_\Lambda(X)) = \Psi_\Lambda(X)$) (Crespo, Serra, and Schafer 1999). Anti-extensive attribute filters are considered as attribute openings or thinnings, depending on whether the criterion is, respectively, increasing or not (Breen and Jones 1996).

Grey-level connected filters can be constructed by the binary connected filters using the notion of threshold decomposition (Maragos and Ziff 1990; Vincent 1993). Given a grey-level image f: V→Z, thresholding f in an increasing order from h_{min} to h_{max} generates a stack of nested binary sets. Each binary image at level h is denoted by

$$T_h(f) = \{x \in V | f(x) \geq h\}, \tag{2}$$

and for any two levels, $h_1 < h_2 \Rightarrow T_{h_1}(f) \supseteq T_{h_2}(f)$.

Thus, grey-level connected filter can be given by the binary connected filter of each level. The response of the greyscale counterpart of a binary increasing filter Ψ_Λ on each point x of image f is denoted by

$$\Upsilon_\Lambda(f)(x) = \sup\{h | x \in \Psi_\Lambda(T_h(f))\}. \tag{3}$$

The operator Υ_Λ assigns each point of the original image the highest threshold at which it still belongs to a connected foreground which satisfies an attribute criterion Λ. Nonincreasing (increasing) attributes can also be used to define greyscale nonincreasing (increasing) filters (Breen and Jones 1996).

2.3. *Max-tree algorithm*

For grey-level image, connected filters can be implemented efficiently by tree-based algorithms (Salembier, Oliveras, and Garrido 1998; Jones 1999). Max-tree algorithm is a typical example introduced by Salembier, Oliveras, and Garrido (1998) for anti-extensive connected filtering. Given a grey-level image f, the tree structure reflects the nesting order of its connected components Q_h^i. The nodes C_h^i, addressed by their level h and index *i*, correspond to sets of pixels for which there exists a unique mapping to connected components:

$$C_h^i = \{x \in Q_h^i \mid f(x) = h\}. \tag{4}$$

Each node of the max-tree points to its parent at level h′< h, except for the root node. The root node at level h_{min} points to itself. Every parent inherits the attribute of its descendants, which makes the computation of connected component attributes simple. Inheritance is a simple accumulation in the case of increasing attributes such as area or volume.

As above, the nodes C_h^i are just a subset of the connected components Q_h^i. Actually, the connected components Q_h^i are equivalent to the set of pixels belonging to C_h^i and all their descendant nodes. In this paper, the nodes C_h^i correspond to the connected components Q_h^i straightforwardly, which was proposed by Jones (1999). In such a case, for nodes C_h^i, there exist nodes C_{h+1}^n such that $C_{h+1}^n \subseteq C_h^i$, and C_{h+1}^n is the descendant of C_h^i. C_0^1 at the minimum grey level in the image is the entire image domain and called the root of a tree. A node that is not linked to another component at a higher grey level is called a leaf node of the tree. Thus, the set of nodes and the links between them form the structure of the tree.

The grey-level connected filters may be implemented using the following tree filter, which classifies every tree node C_h^i using the simple rule:

$$C_h^i \text{ is } \begin{cases} \text{active, if } C_h^i \text{satisfies criterion } \Lambda, \\ \text{not active, otherwise.} \end{cases} \tag{5}$$

In this formula, a morphological opening is obtained when increasing criteria are used and a morphological thinning is obtained while nonincreasing criteria are used (Breen and Jones 1996).

The max-tree is usually constructed by flood-filling (Salembier, Oliveras, and Garrido 1998) or union-find (Najman and Couprie 2006) approach. The flood-filling approach is usually based on a hierarchical queue. It performs a depth-first scan of the tree, starting at the lowest grey level of the image which represents the root of the tree, and moving upwards in greyscale. The union-find approach has a low theoretical complexity, but it is slower than the hierarchical queue approach (Salembier and Wilkinson 2009).

3. Building segmentation from lidar data

In this paper, the general principle of building extraction from lidar data is based on the slope difference between ground and building features. Connected operators are involved to extract buildings effectively and straightforwardly. The outline of the method is given over the following three steps.

(1) *Initialization* constructs a regular grid over the input lidar point cloud.
(2) *Extraction of building candidate regions* is performed by area-based filtering on max-tree representation of lidar-generated DSM.
(3) *Removing vegetation regions* is done by thresholding minimal area and maximum normalized difference vegetation index (NDVI) value of building regions.

3.1. *Initialization*

There are three main neighbourhood representation approaches for lidar point clouds (Filin and Pfeifer 2005): (1) rasterization of the points which was applied to filtering (Zhang et al. 2003; Chen et al. 2007; Shao and Chen 2008, Meng et al. 2009b; Liu et al. 2012, Li et al. 2013; Pingel, Clarke, and Mcbride 2013; Mongus, Lukač, and Žalik 2014) and building extraction (Zhang, Yan, and Chen 2006; Meng, Wang, and Currit 2009a; Kabolizade, Ebadi, and Ahmadi 2010; Huang, Brenner, and Sester 2013; Mongus, Lukač, and Žalik 2014) from lidar data; (2) triangulation of the points mainly applied to filtering (Axelsson 2000); and (3) storage of the points in buckets (Kraus and Pfeifer 1998),

rectangular cells containing 100–1000 points. In this research, the rasterization method is applied to building extraction from lidar points. Three criteria of choosing this method are as follows: (1) simple to manage, and the spatial and topological relationships among points are easy to handle; (2) mature image processing algorithms can be applied to lidar data; and (3) little deviations, if the resolution of rasterization is similar to the density of lidar data.

Lidar raw point data are shown in Figure 1(*a*), and connectivity between points is established by the construction of a grid G with a finite rectangular subset I. The extent of I is related to bounding box of lidar points and p denotes a grid point. The construction of G is done by the following three steps (Mongus, Lukač, and Žalik 2014).

(1) R_G defines the resolution of G, estimated according to the lidar data density *D*.
(2) *g*[p] Is the value of g at p given by the lowest elevation point contained within the corresponding grid cells.
(3) p* Denotes an undefined grid point obtained when no points are contained within the corresponding grid cell. In this case, *g*[p*] is estimated by the nearest neighbour interpolation method to guarantee the authenticity of the original data.

In addition, outliers of lidar data, including high outliers and low outliers, should be removed. Low outliers originate from multi-path errors and that of laser range finder,

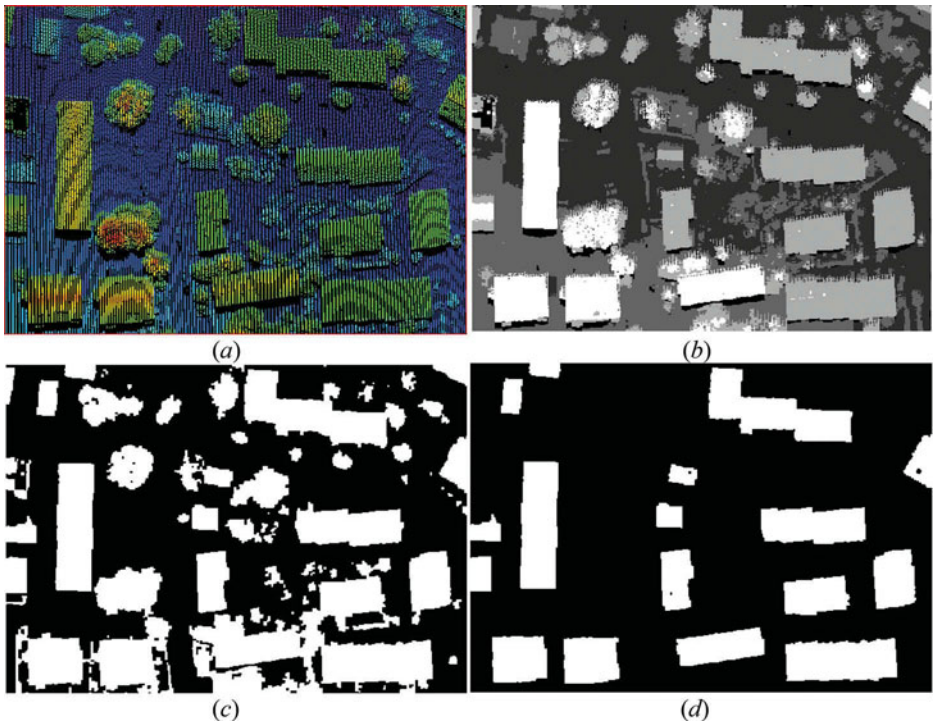

Figure 1. The process of building regions extraction: (*a*) raw lidar points which are cut out from ISPRS benchmark data set in Vaihingen; (*b*) grid data interpolated by lidar points; (*c*) building candidate regions; and (*d*) final extracted building regions.

while high outliers usually result from pulses hitting birds, aircrafts, and so on (Sithole and Vosselman 2004). High outliers can be removed by the morphological opening (Chen et al. 2007). In contrast, morphological closing can remove low outliers of lidar data (Mongus and Žalik 2012), but it will connect two close buildings, if the buildings of test area are concentrated. So, the low outliers E are detected as follows (Li et al. 2013):

$$\mathrm{E} = \left\{\mathrm{p} | \rho^{+}(\mathrm{p}) \rangle t_1; \mathrm{sum}\left\{\mathrm{p}_i \in \mathrm{N_p} | \mathrm{abs}(g[\mathrm{p}_i] - g[\mathrm{p}]) < t_2\right\} < t_3\right\}, \tag{6}$$

where $\rho^{+}(\mathrm{p})$ refers to the half gradient by dilation of grid point p, whose threshold is t_1. $\mathrm{abs}(g[\mathrm{p}_i] - g[\mathrm{p}])$ is the absolute value of height difference between p and p_i which is a neighbouring pixel of p in the neighbourhood $\mathrm{N_p}$, and t_2 is its threshold. t_3 is the threshold of the sum of points near p. $\rho^{+}(\mathrm{p})$ is defined as the difference between the dilated value and the original value:

$$\rho^{+}(\mathrm{p}) = \delta_{\mathrm{B}}(\mathrm{G})[\mathrm{p}] - g[\mathrm{p}], \tag{7}$$

where $\delta_{\mathrm{B}}(\mathrm{G})[\mathrm{p}]$ refers to the dilation value of p in grid G with a structuring element B (3×3 square).

After removing outliers of lidar data, the value of outlier will be recovered by the nearest neighbour interpolation method. Finally, as shown in Figure 1(*b*), the lidar-derived DSM is obtained by initializing from lidar point cloud.

3.2. *Extraction of building candidate regions*

The progressive morphological filtering (Zhang et al. 2003) is a common filtering method applied to lidar-derived DSM, in which buildings are extracted from elevations of each pixel obtained by applying morphological filters with increasing size of the structuring element (Zhang, Yan, and Chen 2006; Chen et al. 2007; Li et al. 2013; Pingel, Clarke, and Mcbride 2013; Mongus, Lukač, and Žalik 2014). Compared with the progressive morphological filtering, the building extraction method using connected operators works based on area rather than pixel, which makes building region extraction effective and straightforward.

Lidar-derived DSM can be considered as a grey-level image, so the grey-level connected operators can be applied to extract building regions. At first, threshold decomposition is transformed to grid G. Thresholding grid G in an increasing order from $\mathrm{h_{min}}$ to $\mathrm{h_{max}}$ will generate a stack of nested binary sets:

$$\mathrm{T_h}(\mathrm{g}) = \{\mathrm{p} \in \mathrm{I} | g[\mathrm{p}] \geq \mathrm{h}\}. \tag{8}$$

However, to remove the small object and the plane with small height in the process of filtering for building extraction from lidar-derived DSM, a stack of nested binary sets are usually generated from the value around the average elevation rather than $\mathrm{h_{min}}$.

Then, the max-tree is constructed. The area difference of one parent node C_k^f and its child node $\widehat{C}_k^f$ is utilized to discriminate building regions. So, we only need to know the relation between the parent node C_k^f and its child node $\widehat{C}_k^f$. Similar to the flood-filling approach, the max-tree in this paper is performed in increasing order of level of grid G, starting at the lowest level of the grid. In addition, to separate building from other objects completely, the attribute-space connectivity (Wilkinson 2007) is introduced to

each level of grid G, namely that each level of gird G is clustered by the elevation value of each grid. Thus, each node of tree represents a clustered region of each level in grid G.

Once the max-tree has been established, the filtering criterion is introduced to analyse each node and takes a decision on the elimination or preservation of the node (Salembier, Oliveras, and Garrido 1998). Based on the slope difference of building and ground, an area difference–based filtering criterion is introduced. The filtering criterion is defined as:

$$\Delta(\mathrm{A}) = C_k^{f\mathrm{A}} - \widehat{C_k^f}^{\mathrm{A}}. \tag{9}$$

$C_k^{f\mathrm{A}}$ is the area of C_k^f, $\widehat{C_k^f}^{\mathrm{A}}$ the area of $\widehat{C_k^f}$, and $\Delta(\mathrm{A})$ the difference of two. Suppose that T_{A_1} is the threshold of $\Delta(\mathrm{A})$. Namely, if the value of $\Delta(\mathrm{A})$ is less than T_{A_1}, the corresponding connect components will be considered as the candidate building object, which is called as the min filtering rule (Salembier and Wilkinson 2009). In addition, although the area is decreasing attribute, the area difference is not. This means that the area difference between a child node and its parent node can be above the given threshold, while the area difference between its parent node and grandparent node is below the threshold and will make the filter unstable (Salembier and Wilkinson 2009). To solve this problem, the nodes from the node C_k^f to the leaf node are all classified active node, if the node C_k^f satisfies the citation. The results of candidate building extraction are shown in Figure 1(*c*).

In fact, the value of $\Delta(\mathrm{A})$ is related to the inclination degree of one object (building or hill). As shown in Figure 2, suppose that building is an ideal cylinder, hill is an ideal parabolic body, and areas S_1 and S_2 are two connected components of hill corresponding to two nodes of max-tree. Areas S_3 and S_4 are two connected components of the building. Suppose that areas $S_1, S_2, S_3,$ andS_4 are all the standard circles, and r_1 and r_2 are the radii of the areas S_1 and S_2, respectively; d is the interval of two adjacent elevation levels and e the inclination degree of the hill, respectively. In such a case, $\Delta(\mathrm{A})$ is the area difference between the areas S_1 and S_2:

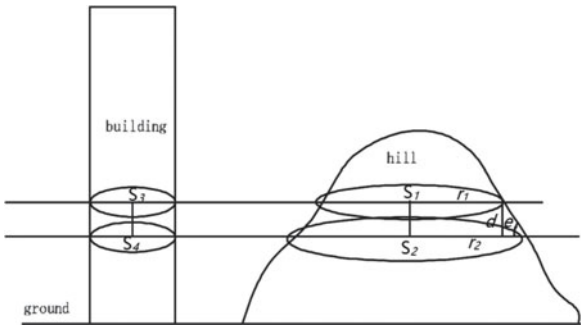

Figure 2. The schematic diagram of building extraction: 'S_1' and 'S_2' are two connected components of hill; 'r_1' and 'r_2' are the radii of the area S_1 and S_2, respectively; '*d*' and '*e*' are the interval of two adjacent elevation levels and the inclination degree of object, respectively; S_3 and S_4 are two connected components of building.

$$\begin{aligned}\Delta(\mathrm{A}) &= \pi {r_2}^2 - \pi {r_1}^2 = \pi(r_1 + d\cot e)^2 - \pi {r_1}^2 \\ &= \pi d\cot e(2r_1 + d\cot e).\end{aligned} \tag{10}$$

Thus, the value of $\Delta(\mathrm{A})$ is related to the values of r_1, e, and d. It is known to us that building size is smaller compared with the ground, and building has greater inclination degree. So, the corresponding value $\Delta(\mathrm{A})$ of building is smaller than ground. As shown in Figure 2, the areas of S_3 and S_4 are almost equal; d is the input parameter which will also affect the value of $\Delta(\mathrm{A})$. The value of T_{A_1} is related to the maximum size of the building object, the maximum slope of the ground object, and the input parameter d.

3.3. *Removing vegetation regions*

Building candidate regions contain buildings and vegetation which should be removed. Usually, spectrum, area, elevation, roughness, and the number of echoes are adopted to distinguish building and vegetation areas (Lee, Lee, and Lee 2008). Although researchers make many efforts to distinguish buildings from trees based on lidar data only (Rottensteiner and Briese 2002; Li et al. 2010; Yang, Xu, and Dong 2013; Mongus et al. 2013; Mongus, Lukač, and Žalik 2014), they have not got a satisfactory result till now. Some complex buildings will be recognized as vegetation using texture of feature, and some high vegetation will also remain if a height threshold is applied to maintain the buildings. Under these conditions, a colour feature based on the image is introduced to discriminate buildings from trees (Li et al. 2010; Kabolizade, Ebadi, and Ahmadi 2010; Vu, Yamazaki, and Matsuoka 2009).

The average NDVI value P_N and area P_A of every region are calculated. The NDVI value of each grid is calculated by the NDVI value of its corresponding pixel in the image:

$$g_{\mathrm{NDVI}}[\mathrm{p}] = \frac{g_{\mathrm{NIR}}[\mathrm{p}] - g_{\mathrm{R}}[\mathrm{p}]}{g_{\mathrm{NIR}}[\mathrm{p}] + g_{\mathrm{R}}[\mathrm{p}]}, \tag{11}$$

where $g_{\mathrm{NIR}}[\mathrm{p}]$ refers to the near-infrared band value of the corresponding image, and $g_{\mathrm{R}}[\mathrm{p}]$ red band value of the corresponding image. If $P_N < T_N$ and $P_A > T_{A_2}$, this region is building or tree. T_N and T_{A_2} are the thresholds of P_N and P_A. The final building regions are as shown in Figure 1(*d*).

4. Extraction of building boundaries

After the extraction of building regions, the boundaries of buildings need to be extracted. It can be divided into two steps: identifying the boundaries and boundary tracking. First, the building grid point adjacent to ground grid point is considered as the boundary point of buildings, and the boundary point must have only two adjacent points. Second, boundary points in one unordered set are tracked in order to find an ordered set of boundary points. Two adjacent boundary points constitute a boundary line, so building boundaries consist of a number of ordered line segments.

4.1. *Boundary identification*

A building region presented by binary image is shown in Figure 3(*a*). The values '0' (black area in Figure 3(*a*)) and '255' (white area in Figure 3(*a*)) represent ground and building, respectively. In the eight neighbourhoods of a '255' grid point, if there is one or more '0' grid points, the '255' grid point is identified as boundary point. To trace boundary points conveniently, each boundary point can and only can have two adjacent points. In the red rectangular areas of Figure 3(*b*), there are boundary points which have three adjacent points. So, as shown in the red rectangular areas of Figure 3(*c*), in the case of ensuring connectivity, we can remove one adjacent point.

4.2. *Boundary tracing*

Once the boundary of building region is identified, it should be tracked before regularization. A simple boundary is a loop where a set of boundary points are connected in a series. However, some buildings have one or more inner cavities so that these buildings have two or more loops.

In addition, the boundary of the raw footprint contains too many details and 'zigzag' noise because of the irregularly spaced point measurements and the grid-based interpolation. Thus, a line simplification method is introduced to reduce the noise of the raw footprint. In this research, an algorithm originally proposed by Zhao and Saalfeld (1997) is modified to perform the line simplification. The great advantage of this algorithm is

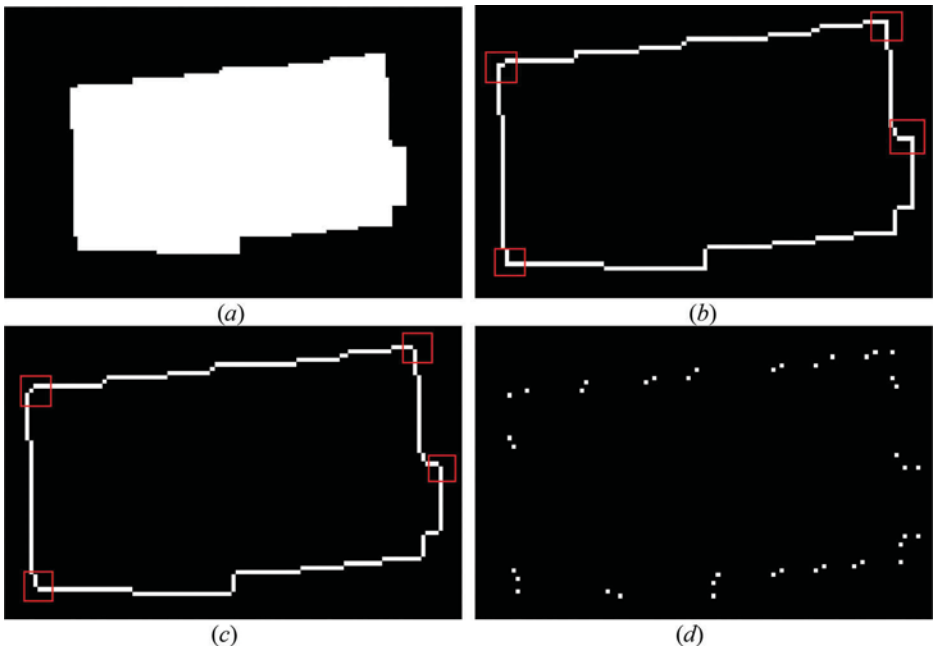

Figure 3. Principles of building boundary determination: (*a*) building region; (*b*) identification of building boundary and boundary points which have three adjacent points in the red rectangular areas; (*c*) removing redundant boundary grid points in the red rectangular areas; and (*d*) result of boundary tracing.

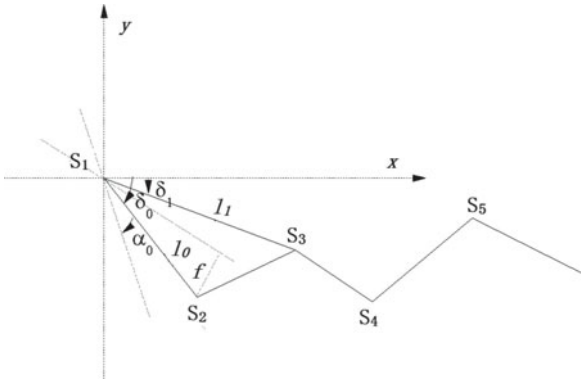

Figure 4. Line simplification using the 'sleeve' algorithm: points $S_1, S_2, \ldots, S_5$ denote the boundary grid point of one building; l_0 and l_1 are the lengths of line segments S_1S_2 and S_1S_3; δ_0 is an angle between line segment S_1S_2 and positive direction of axis x; δ_1 is an angle between line segment S_1S_3 and positive direction of axis x; $\Delta\alpha_0$ is calculated as $\tan^{-1} f/2l_0$; f is the input parameter which indicates how far a point deviating from a line can be kept as a key point.

that it can process points in sequence, which is very suitable for processing boundary points when they are extracted from raster format to vector (Ma 2004).

For simple building boundaries, starting from the lower left corner point, it is traced anticlockwise. The process can be described as follows.

(1) As shown in Figure 4, points $S_1, S_2, \ldots, S_5$ denote the boundary grid point of one building, and f is the input parameter, which indicates how far a point deviating from a line can be kept as a key point.
(2) The beginning point $S_i(S_1)$ is determined and $S_{i+1}(S_2)$ is the right neighbour point of $S_i(S_1)$. The length l_0 and direction angle δ_0 of line segment $S_iS_{i+1}(S_1S_2)$ are calculated, and δ_0 is an angle between line segment $S_iS_{i+1}(S_1S_2)$ and positive direction of axis x.
(3) The direction range α_0 at current point $S_i(S_1)$ is calculated according to the line-segment length l_0 and parameter f. The range of α_0 is given by $\delta_0 \pm \Delta\alpha_0$. $\Delta\alpha_0$ is calculated as $\tan^{-1}\frac{f}{2l_0}$.
(4) $S_{i+2}(S_3)$is the right neighbour point of $S_{i+1}(S_2)$. In the same way, the length l_1 and direction angle δ_1 of line segment $S_iS_{i+2}(S_1S_3)$ are calculated. The direction range of $\alpha_1$is given by $\delta_1 \pm \Delta\alpha_1$. $\Delta\alpha_1$ is calculated as $\tan^{-1}\frac{f}{2l_1}$.
(5) If the direction δ_1 is within the calculated direction range α_0, the point $S_{i+1}(S_2)$ is discarded because it is not a key point. Then, a new direction range of line segment $S_iS_{i+2}(S_1S_3)$ is generated as the intersection of the direction range α_0 and α_1. The new direction α_0 for further testing is $[\max(\delta_0 - \Delta\alpha_0, \delta_1 - \Delta\alpha_1), \min(\delta_0 + \Delta\alpha_0, \delta_1 + \Delta\alpha_1)]$. Go back to step 2, S_i=S_1 S_{i+1}= S_3.
(6) If direction δ_1 is out of the direction range α_0, the point $S_{i+1}(S_2)$ is kept in the generalized line as a key point. The point $S_{i+1}(S_2)$ is taken as the first point of a new line segment and the point $S_{i+1}(S_3)$ is taken as the second point for the next simplification process. Repeat the procedure in steps 2–6 until the last point.

The result of simple building tracing is shown in Figure 3(*d*). For the building which has one or more inner cavities, the tracing process of the outer boundary is the same as the process described above, while an inner boundary is traced clockwise commencing from the lower left corner point.

After the tracing and simplification of building boundaries, each building boundary consists of several line segments whose length and direction can be achieved. The number and length of boundary line segments are determined by parameter *f*.

5. Boundary regularization

Figure 6(*a*) shows the traced roof boundary line segments of a practical building scene (f = 1 pixel). As can be seen, there is an obvious irregularity or noise in the lidar-derived building boundary line segments. Thus, the first step of the proposed regularization method is to merge the extracted boundary line segments and find the principal directions of buildings to regularize the boundary line segments of buildings. For the second step, the direction of each boundary line segment is classified based on principal directions of building.

5.1. *Confirmation of principal directions*

Though the line simplification method is introduced in the process of boundary tracing, there is still an obvious irregularity or noise in the lidar-derived building boundary line segments. Thus, in the condition of not changing the outline of building, the lines in the same direction and that of small length will be merged. For the line segment L_i, the process of line merging is as follows.

- *Merged by length*: l_i and l_{i+1} are the lengths of line segments L_i and L_{i+1}. If $l_i < T_L$ (T_L is a threshold of length), line segment L_i is merged with L_{i+1} and $l_i = l_i + l_{i+1}$. The building boundary lines are merged successively, as they are shown in Figure 6(*b*).
- *Merged by direction*: $\Delta\partial_0$ is the directional difference of line segment L_i and L_{i+1}. If $\Delta\partial_0 < T_D$ (T_D is a directional threshold), boundary line segment L_i will be merged with L_{i+1}, then comparing L_i with L_{i+2} successively. If $\Delta\partial_0 \geq T_D$, the directional difference $\Delta\partial_1$ of L_{i+1} and L_{i+2} is calculated first and compared with T_D. The steps above are followed to merge the boundary line segments in turn (Figure 6(*c*)).

In this paper, we consult the method mentioned by Zhang, Yan, and Chen (2006) to confirm the main direction of buildings, since it is very robust. The major direction of the buildings will be defined in accordance with the longer building segments. Let x' and y' represent possible dominant directions in a 2D xy-coordinate system (Figure 5). The dominant directions x' and y' are related to the coordinate systems x and y through an anticlockwise rotation by an angle q ($0 \leq q < 90$). Therefore, the key step to estimate the dominant directions is to find the rotation angle q. Assuming that the anticlockwise intersection angle between a line segment and the x-axis is t_i ($0 \leq t_i < 180$), we define

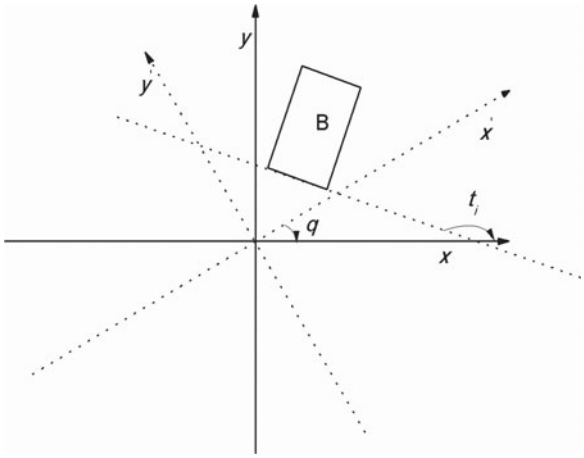

Figure 5. 'B' represents a building outline; the coordinate systems x' and y' are anticlockwise rotation of the coordinate systems x and y by an angle q; t_i is the anticlockwise intersection angle between a line segment of a building footprint and the axis x.

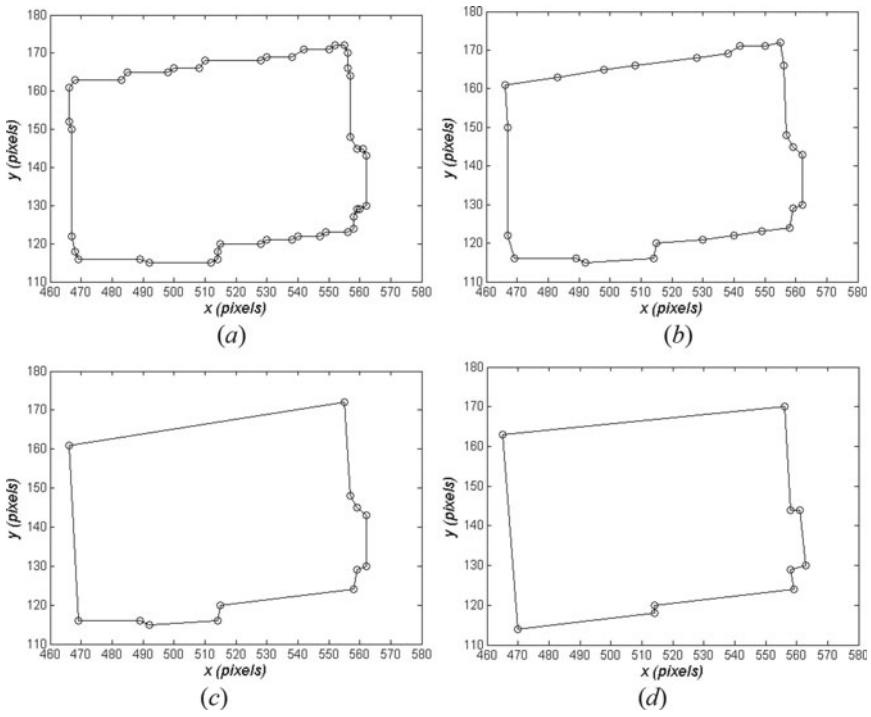

Figure 6. The process of boundary regularization: (*a*) boundary line segments after tracing; (*b*) merging the line segments of small length; (*c*) merging the line segments of same direction; and (*d*) boundary line segments after regularizing.

$$W = \sum_{i=1}^{N} g(l_i) f(t_i, q), \tag{12}$$

where N is the total number of building boundary line segments, l_i is the ith boundary line-segment length, $g()$ is the weight function based on l_i, and $f()$ is the weight function based on t_i and q. The dominant building directions can be estimated through finding an optimum q so that W will reach a minimum. Functions $f()$ and $g()$ are presented as follows.

$$g(l_i) = \frac{l_i}{\sum_{i=1}^{N} l_i}. \tag{13}$$

$$f(t_i, q) = \begin{cases} \min(|t_i - q|, 90 - |t_i - q|)/45 : |t_i - q| \le 90 \\ \min(180 - |t_i - q|, |t_i - q| - 90)/45 : |t_i - q| > 90 \end{cases}. \tag{14}$$

5.2. *Regularization of direction*

We classify the direction of building line segments after confirming the main direction. Suppose $D_h = q$ is the horizontal main direction, $D_v = q + \pi/2$ the vertical main direction, $d_i (0 \le d_i < 180) \text{and} l_i (i = 1, 2, \ldots, N)$ the direction and length of the ith building line segments, and N the number of the building line segments, then classifying d_i:

$$d_i = \begin{cases} D_h | D_h - d_i | < d_t \text{ or } |D_h - \pi + d_i| < d_t, \\ D_v | D_v - d_i | < d_t \text{ or } |D_v - \pi + d_i| < d_t, \\ d_i \text{ others}. \end{cases} \tag{15}$$

d_t is the threshold value we set. If $|D_h - d_i| < d_t$, d_i is close to the horizontal main direction D_h and let $d_i = D_h$; if $|D_v - d_i| < d_t$, d_i is close to the vertical main direction D_v and let $d_i = D_v$; otherwise, d_i is oblique and remains unchanged. According to the classification of building boundary line segments, we can regularize the building boundary line segment, as shown in Figure 6(*d*).

6. Experiments and evaluation

The proposed method was tested with three test data sets in Vaihingen from 'ISPRS benchmark dataset'. The lidar data is acquired by Leica Geosystems using a Leica ALS50 system with 45° field of view and a mean flying height above ground of 500 m. The median point density is 6.7 points/m^2. The area of buildings is 50–700 m^2. The buildings in 'area 1' have skew angles with the flight direction, and the buildings in 'area 2 and area 3' are mostly parallel or perpendicular to the flight direction.

6.1. *Parameter setting*

In this section, the parameters of experiment are set for three areas. The lidar data of test area have relatively high density, so we let $R_G = 0.3$m. Moreover, in order to remove outliers of lidar points effectively, let t_1 = 100 m, t_2 = 0.5 m, and t_3 = 4. The value of T_{A_1}

can be estimated by Equation (10). For Equation (10), r_1 is related to the maximum size of building object and e is related to the maximum slope of ground object. So, we let $r_1 = 50$ pixels, $e = 30°$ and $d = 0.1$ m for three test areas, and $T_{A_1} = 55$pixels are achieved. Parameter T_{A_2} is calculated by $T_{A_2} = S_m/0.09$ and S_m is the minimum size of building object in test area. Parameter T_N is fitted based on the luxuriant degree of vegetation regions. To simplify the building boundary under the condition of not changing the outline of boundary, we let $f = 1$ pixel, $T_L = 3$ pixels, $T_D = \pi/10$, and $d_t = \pi/10$.

6.2. *Accuracy and performance evaluation of building extraction*

In this section, the performance of building extraction method newly proposed within this paper will be compared with the method based on DMPs which is developed from morphology filter by Mongus (2014).

The execution times of the method in this paper and the method based on DMPs were measured on AMD Phenom (tm) II X6 1055 T Processor 2.80 GHz with 8 GB of main memory. The accuracy of the method proposed within this paper was evaluated according to the ISPRS reference data. Therefore, the completeness CP (%), correctness CR (%), and quality Q (%) metrics were used, as proposed by Rutzinger, Rottensteiner, and Pfeifer (2009). The results of the execution times and evaluation of the method in this paper are shown in Table 1, which were compared with the method based on DMPs.

The method based on DMPs is executed by pixel. So, it has a long execute time and is affected by the size of the contained buildings in test area. The method in this paper is much more effective than the method based on DMPs since it is performed based on area; what is more, it would not be influenced by the size of the contained buildings.

As shown in Table 1, the efficiency of the method in this paper is over 10 times better than that of the method based on DMPs, but they are almost equal in accuracy. For the accuracy of buildings extraction results by the method in this paper, the correctness is a little bit better while the completeness is a little bit worse in area 1, which is mainly caused by the missing extraction of low buildings (Figure 7(*a*) A); the correctness is a little bit worse while the completeness is a little bit better in area 2, for the vegetation is connected to and recognized as a building (Figure 7(*b*) B); and the correctness and completeness are both a little bit worse in area 3 when compared with the method based on DMPs, which is caused by both the missing extraction of low buildings (Figure 7(*c*) D and E) and the vegetation connected to and recognized as a building (Figure 7(*c*) C and F).

Table 1. The results of the execution times and evaluation of the method in this paper compared with the method based on DMPs.

		Per-pixel			Per-object			Per-object for objects > 50 m^2			
Test case	Method	CP	CR	Q	CP	CR	Q	CP	CR	Q	Time (s)
Area 1	DMPs method	90.3	91.7	83.5	86.5	93.9	81.9	100.0	96.6	96.6	188.84
	Our method	89.4	94.5	84.9	83.8	93.8	79.4	100.0	100.0	100.0	17.55
Area 2	DMPs method	89.9	97.8	88.1	78.6	91.7	73.4	100.0	100.0	100.0	172.54
	Our method	91.0	95.0	86.8	78.6	91.7	73.3	100.0	100.0	100.0	6.44
Area 3	DMPs method	88.9	96.2	85.9	76.8	95.6	74.2	97.4	100.0	97.4	215.94
	Our method	87.7	94.5	83.4	73.2	97.7	72.0	94.9	100.0	94.9	8.69

'CP', 'CR', and 'Q' are completeness, correctness, and quality metrics, respectively.

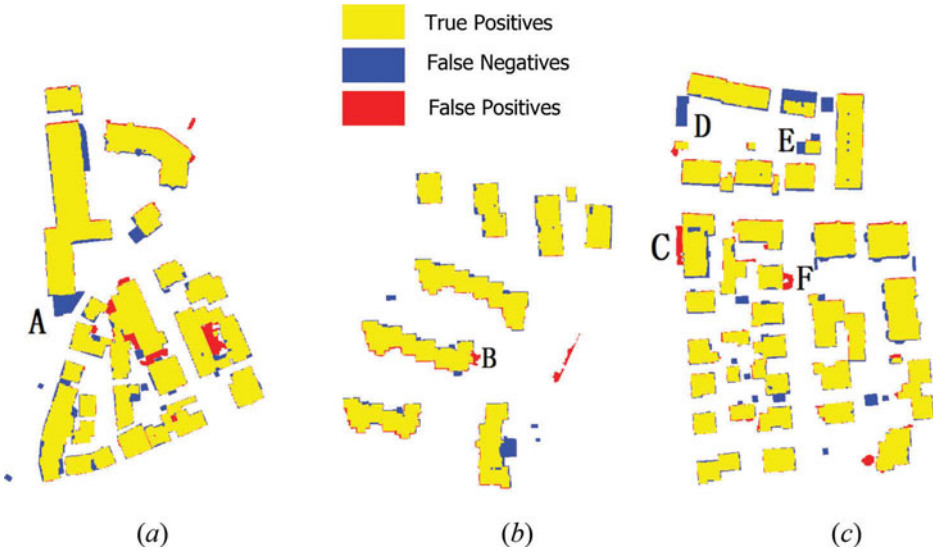

Figure 7. Evaluation results of building detection in the three test areas.

6.3. *Accuracy evaluation of buildings boundary*

Figures 8–10 show regularized buildings in three test areas of Vaihingen, respectively. In these figures, the regularized building boundaries are overlaid on the lidar surface model; lidar boundary points labelled by number are selected from lidar raw points manually; d is the average offset distance from those points to the corresponding boundary line segments, and σ is the standard deviation of the offset distance.

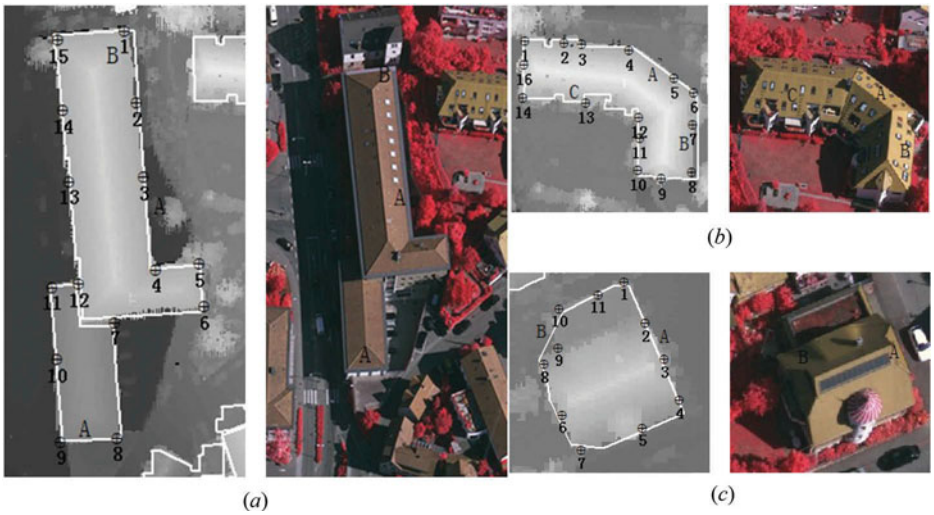

Figure 8. Regularized building boundary, corresponding image and quality in area 1: (*a*) d = 0.35 m, $\sigma = \pm 0.43$ m; (*b*) d = 0.43 m, $\sigma = \pm 0.57$ m; and (*c*) d = 0.45 m, $\sigma = \pm 0.57$ m. Building 'a' is simpler than buildings 'b' and 'c'. So, the average offset distances of buildings 'b' and 'c' are greater than the average offset distances of building 'a'.

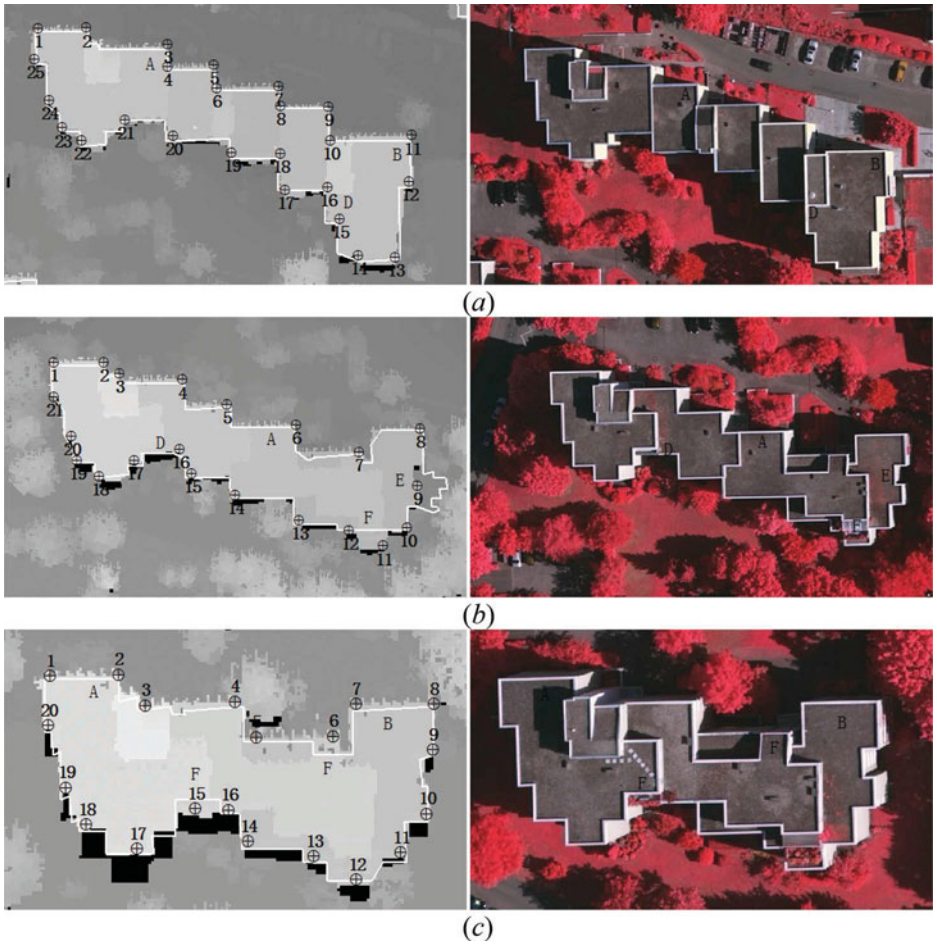

Figure 9. Regularized building boundary, corresponding image and quality in area 2: (*a*) $d = 0.54$ m, $\sigma = \pm 0.64$ m; (*b*) $d = 0.72$ m, $\sigma = \pm 0.93$ m; and (*c*) $d = 0.60$ m, $\sigma = \pm 0.74$ m. Buildings 'a', 'b', and 'c' are all complex, so the average offset distances of the three buildings are all large. In addition, the average offset distances of buildings 'b' and 'c' are greater, which is caused by misleading points.

Several observations can be made based on the results in Figures 8–10. It is first seen that almost all building boundary line segments are very well determined. The regularized boundary fits to the lidar boundary points and reflects the buildings' shape. The building outline provides an authentic appearance comparing to the images and the lidar surface model. Second, many minor rectilinear features, for example, the short right-angle line segments labelled as A, are determined correctly through the regularization process. This forms the fine details in the determined building boundary, which can possibly be inferred from the lidar data. As shown by the B labels, the boundary line segments have a large shift from lidar boundary points due to the regularization of line segments. At the C labels of Figure 8(*b*), the complex structure of building will introduce errors in the process of regularization. And at the D labels of Figure 9(*a*) and (*b*), the errors are led into by the interpolation of lidar DSM. Finally, at the E and F labels of Figures 9(*b*), (*c*), and 10(*b*), the errors are led to by the errors of building detection results.

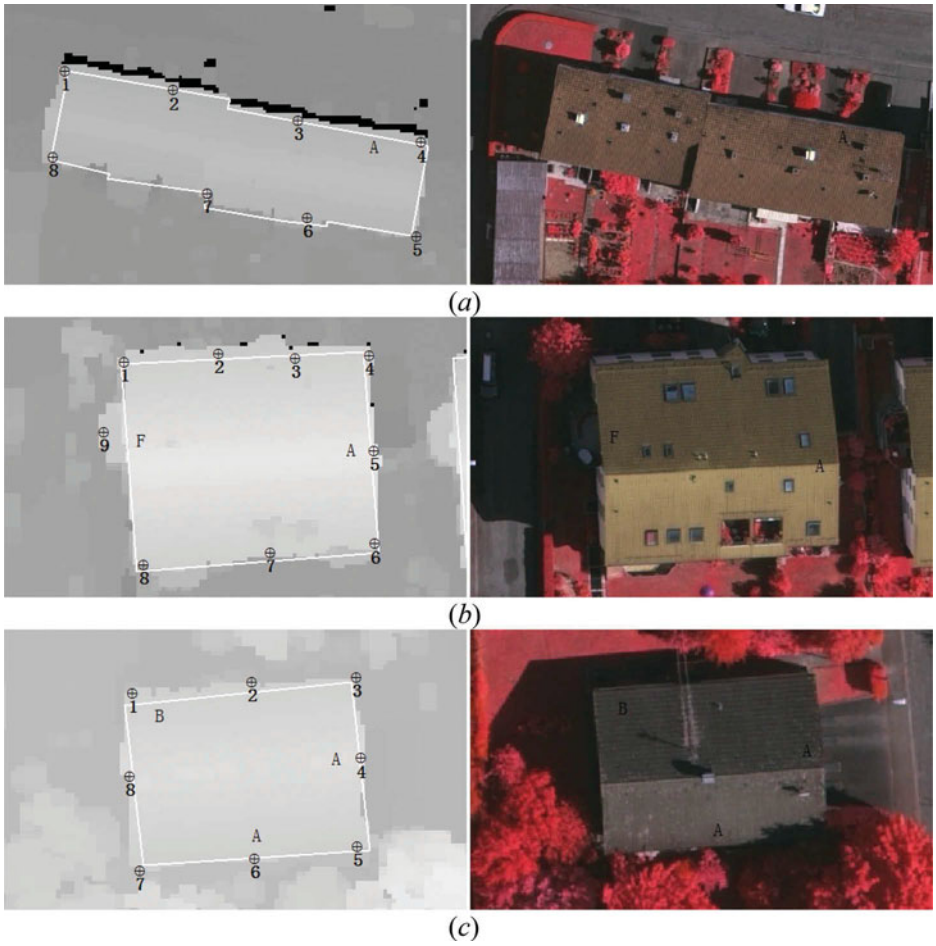

Figure 10. Regularized building boundary, corresponding image and quality in area 3: (*a*) $d = 0.28$ m, $\sigma = \pm 0.34$ m; (*b*) $d = 0.52$ m, $\sigma = \pm 0.69$ m; and (*c*) $d = 0.35$ m, $\sigma = \pm 0.42$ m. Buildings 'a', 'b', and 'c' are all simple, so the average offset distances of the three buildings are all small. The average offset distances of building 'b' are greater, which is caused by misleading points.

Table 2 lists the offset values of lidar boundary points from boundary line segments obtained from nine buildings of three test areas. The measurements are used to quantitatively evaluate the fitness of the regularized building boundary to the lidar points. Corresponding to Figures 8–10, (A), (B), and (C) represent three buildings in each area; 'Number' is the serial number of the boundary points in every building. 'Mean1' and 'Std1' denote the average offset distance and standard deviation of the offset distance of the boundary points including misleading points (bold value in Table 2) resulting from building extraction, while 'Mean2' and 'Std2' denote the average offset distance and standard deviation of the offset distance of the boundary points excluding misleading points. As we can see from the data, the more complicated the building is, the larger the offset value will be. In the test data of area 3, the buildings are simple, so the average offset value of buildings from 0.2 to 0.4 m is small except for the misleading

Table 2. The offset values of buildings in three areas: corresponding to Figures 8–10, (A), (B), and (C) represent three buildings in each area.

	Area 1			Area 2			Area 3		
Number	(A) (m)	(B) (m)	(C) (m)	(A) (m)	(B) (m)	(C) (m)	(A) (m)	(B) (m)	(C) (m)
1	0.10	0.06	0.44	0.67	0.56	0.41	0.26	0.19	0.73
2	0.39	0.63	0.07	0.74	0.68	0.55	0.11	0.43	0.66
3	0.14	0.59	0.37	0.93	0.22	0.49	0.11	0.24	0.47
4	0.34	0.55	0.09	0.14	0.68	0.61	0.23	0.48	0.11
5	0.29	0.02	0.31	0.93	0.52	0.54	0.59	0.25	0.30
6	0.44	0.09	0.65	0.29	0.68	**2.19**	0.63	0.22	0.05
7	0.89	1.12	0.56	0.86	0.48	0.74	0.06	0.64	0.36
8	0.08	1.20	0.42	0.12	0.35	0.31	0.22	0.49	0.16
9	0.38	0.40	1.40	0.35	**1.96**	0.02	–	**1.72**	–
10	0.19	0.01	0.49	0.11	0.04	0.08	–	–	–
11	0.38	0.56	0.18	1.13	**2.55**	0.54	–	–	–
12	0.19	0.20	–	0.26	0.11	0.14	–	–	–
13	0.05	0.57	–	0.41	0.86	0.73	–	–	–
14	0.43	0.03	–	0.95	0.57	0.87	–	–	–
15	0.89	0.49	–	0.95	0.71	**0.94**	–	–	–
16	–	–	–	0.95	1.09	0.41	–	–	–
17	–	–	–	0.20	1.02	0.57	–	–	–
18	–	–	–	1.03	0.24	0.80	–	–	–
19	–	–	–	0.36	0.45	0.61	–	–	–
20	–	–	–	0.89	1.12	0.46	–	–	–
21	–	–	–	0.11	0.22	–	–	–	–
22	–	–	–	0.29	–	–	–	–	–
23	–	–	–	0.28	–	–	–	–	–
24	–	–	–	0.44	–	–	–	–	–
25	–	–	–	0.15	–	–	–	–	–
Mean1 (m)	0.35	0.43	0.45	0.54	0.72	0.60	0.28	0.52	0.35
Std1 (m)	0.43	0.57	0.57	0.64	0.93	0.74	0.34	0.69	0.42
Mean2 (m)	–	–	–	–	0.56	0.49	–	0.37	–
Std2 (m)	–	–	–	–	0.64	0.55	–	0.40	–

'Number' is the serial number of the boundary point in each building. 'Mean1' and 'Std1' denote the average offset distance and standard deviation of the offset distance of the boundary points including misleading points (bold values) resulting from building extraction, while 'Mean2' and 'Std2' excluding misleading points.

points. The average offset values are located between 0.3 and 0.6 m in areas 1 and 2 where some buildings are complex. The offset values of complicated buildings are large while they are small for simple buildings. The buildings extraction results of three test areas are shown in Figure 11.

7. Conclusion

The steps of determining building boundary from lidar data include the following: (1) attribute filters for separating building candidate regions from lidar data; (2) removing vegetation regions from building candidate regions by NDVI value of image; (3) identifying and tracing building boundary; and (4) confirming the main directions of buildings and regularizing the building boundary line segments based on estimated main directions.

Attribute flitters are introduced to detect building regions from lidar data. Three test areas from ISPRS benchmark data are utilized for experiments, and the reference data is used to evaluate the results. Compared with the morphology method based on DMPs, they are almost equal in accuracy, but the proposed method performs more than 10 times in

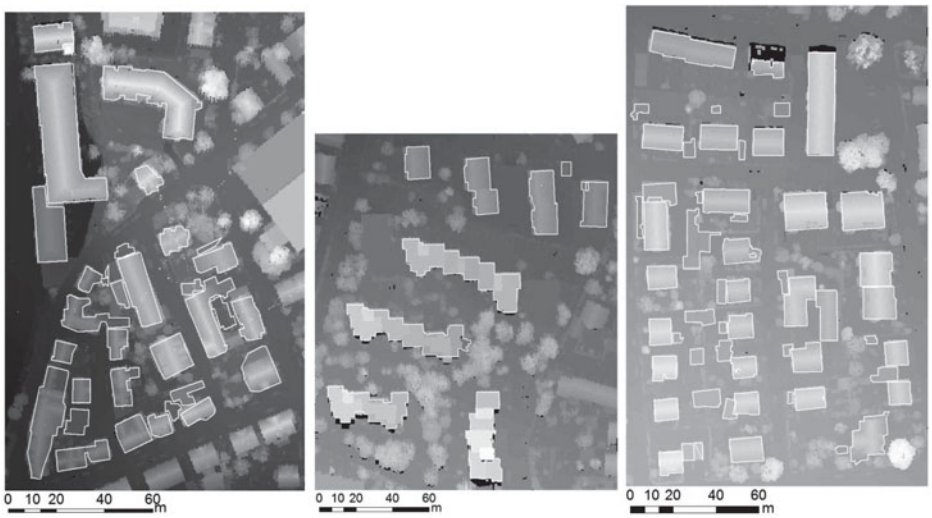

Figure 11. Regularized building boundaries of the three test areas.

efficiency. The errors are mainly caused by the missing extraction of low buildings and the vegetation connected to and recognized as a building. The processes of building boundary tracing and regularization are introduced. For most of the simple buildings, the boundaries can be represented precisely; for the complex buildings which have non-linear boundaries, the non-linear boundaries will be exhibited by the linear form and lead to deviations.

The experiment results show that the method proposed within this paper determined building outlines effectively. The quantitative accuracy analysis indicates that the average offset values from lidar boundary points to boundary line segments is less than 0.6 m ($2R_G$), despite the fact that there are several complex building shapes in Vaihingen area.

Acknowledgements

The Vaihingen data set was created by the ISPRS in the Test Project on Urban Classification and 3D Building Reconstruction. We thank Dr. Markus Gerke, in particular, for evaluating the building detection results in this paper.

Disclosure statement

No potential conflict of interest was reported by the authors.

Funding

This work was supported in part by the National Natural Science Foundation of China [grant number 41322010], [grant number 41171292], and [grant number 41571434].

References

Axelsson, P. 2000. "DEM Generation from Laser Scanner Data Using Adaptive TIN Models." *International Archives of the Photogrammetry, Remote Sensing and Spatial Information Sciences* 33: 110–117.

Baltsavias, E. P. 1999. "A Comparison between Photogrammetry and Laser Scanning." *ISPRS Journal of Photogrammetry and Remote Sensing* 54: 83–94. doi:10.1016/S0924-2716(99)00014-3.

Berger, C., T. Geraud, R. Levillain, N. Widynski, A. Baillard, and E. Bertin. 2007. "Effective Component Tree Computation with Application to Pattern Recognition in Astronomical Imaging." *IEEE International Conference Image Processing* 4: 41–44.

Braga-Neto, U., and J. Goutsias. 2002. "Connectivity on Complete Lattices: New Results." *Computer Vision and Image Understanding* 85: 22–53. doi:10.1006/cviu.2002.0961.

Breen, E. J., and R. Jones. 1996. "Attribute Openings, Thinnings and Granulometries." *Computer Vision and Image Understanding* 64: 377–389. doi:10.1006/cviu.1996.0066.

Cavallaro, G., M. Dalla Mura, J. A. Benediktsson, and L. Bruzzone. 2015. "Extended Self-Dual Attribute Profiles for the Classification of Hyperspectral Images." *IEEE Geoscience and Remote Sensing Letters* 12: 1690–1694. doi:10.1109/LGRS.2015.2419629.

Chen, D., L. Q. Zhang, J. Li, and R. Liu. 2012. "Urban Building Roof Segmentation from Airborne Lidar Point Clouds." *International Journal of Remote Sensing* 33: 6497–6515. doi:10.1080/01431161.2012.690083.

Chen, Q., P. Gong, D. Baldocchi, and G. X. Xie. 2007. "Filtering Airborne Laser Scanning Data with Morphological Methods." *Photogrammetric Engineering & Remote Sensing* 73: 175–185. doi:10.14358/PERS.73.2.175.

Chen, Y., L. Cheng, M. Li, J. Wang, L. Tong, and K. Yang. 2014. "Multiscale Grid Method for Detection and Reconstruction of Building Roofs from Airborne LiDAR Data." *IEEE Journal of Selected Topics in Applied Earth Observations and Remote Sensing* 7: 4081–4094. doi:10.1109/JSTARS.2014.2306003.

Crespo, J., J. Serra, and R. W. Schafer. 1999. "Connected Morphological Operators for Binary Images." *Computer Vision and Image Understanding* 73: 99–120. doi:10.1006/cviu.1998.0703.

Dufour, A., O. Tankyevych, B. Naegel, H. Talbot, C. Ronse, J. Baruthio, P. Dokládal, and N. Passat. 2013. "Filtering and Segmentation of 3D Angiographic Data: Advances based on Mathematical Morphology." *Medical Image Analysis* 17: 147–164. doi:10.1016/j.media.2012.08.004.

Filin, S., and N. Pfeifer. 2005. "Neighborhood Systems for Airborne Laser Data." *Photogrammetric Engineering & Remote Sensing* 71: 743–755. doi:10.14358/PERS.71.6.743.

Heijmans, H. J. A. M. 1999. "Connected Morphological Operators for Binary Images." *Computer Vision and Image Understanding* 73: 99–120. doi:10.1006/cviu.1998.0703.

Huang, H., C. Brenner, and M. Sester. 2013. "A Generative Statistical Approach to Automatic 3D Building Roof Reconstruction from Laser Scanning Data." *ISPRS Journal of Photogrammetry and Remote Sensing* 79: 29–43. doi:10.1016/j.isprsjprs.2013.02.004.

Jones, R. 1999. "Connected Filtering and Segmentation Using Component Trees." *Computer Vision and Image Understanding* 75: 215–228. doi:10.1006/cviu.1999.0777.

Kabolizade, M., H. Ebadi, and S. Ahmadi. 2010. "An Improved Snake Model for Automatic Extraction of Buildings from Urban Aerial Images and LiDAR Data." *Computers, Environment and Urban Systems* 34: 435–441. doi:10.1016/j.compenvurbsys.2010.04.006.

Kilian, J., N. Haala, and M. Englich. 1996. "Capture and Evaluation of Airborne Laser Scanner Data." *International Archives of Photogrammetry and Remote Sensing* 31: 383–388.

Kraus, K., and N. Pfeifer. 1998. "Determination of Terrain Models in Wooded Areas with Airborne Laser Scanner Data." *ISPRS Journal of Photogrammetry and Remote Sensing* 53: 193–203. doi:10.1016/S0924-2716(98)00009-4.

Kurtz, C., N. Passat, P. Gançarski, and A. Puissant. 2012. "Extraction of Complex Patterns from Multiresolution Remote Sensing Images: A Hierarchical Top-Down Methodology." *Pattern Recognition* 45: 685–706. doi:10.1016/j.patcog.2011.07.017.

Kwak, E., and A. Habib. 2014. "Automatic Representation and Reconstruction of DBM from LiDAR Data Using Recursive Minimum Bounding Rectangle." *ISPRS Journal of Photogrammetry and Remote Sensing* 93: 171–191. doi:10.1016/j.isprsjprs.2013.10.003.

Lee, D. H., K. M. Lee, and S. U. Lee. 2008. "Fusion of LiDAR and Imagery for Reliable Building Extraction." *Photogrammetric Engineering & Remote Sensing* 74: 215–225. doi:10.14358/PERS.74.2.215.

Li, Y., H. Y. Wu, H. W. Xu, R. An, J. Xu, and Q. S. He. 2013. "A Gradient-Constrained Morphological Filtering Algorithm for Airborne LiDAR." *Optics & Laser Technology* 54: 288–296. doi:10.1016/j.optlastec.2013.06.007.

Li, Y., L. Zhu, P. Gong, and H. Shimamura. 2010. "A Refined Marker Controlled Watershed for Building Extraction from DSM and Imagery." *International Journal of Remote Sensing* 31 (6): 1441–1452. doi:10.1080/01431160903475373.

Liu, C., J. Li, S. Zhang, and L. Ding. 2012. "A Point Clouds Filtering Algorithm Based on Grid Partition and Moving Least Squares." *Procedia Engineering* 28: 476–482. doi:10.1016/j.proeng.2012.01.754.

Ma, R. 2004. "Building Model Reconstruction from LiDAR Data and Aerial Photographs." Ph. D. dissertation, The Ohio State University, USA.

Maragos, P., and R. D. Ziff. 1990. "Threshold Superposition in Morphological Image Analysis Systems." *IEEE Trans. Pattern Analysis and Machine Intelligence* 15: 498–504.

Meng, X. L., L. Wang, and N. Currit. 2009a. "Morphology-based Building Detection from Airborne LiDAR Data." *Photogrammetric Engineering & Remote Sensing* 75: 437–442. doi:10.14358/PERS.75.4.437.

Meng, X. L., L. Wang, J. L. Silván-Cárdenas, and N. Currit. 2009b. "A Multi-Directional Ground Filtering Algorithm for Airborne LIDAR." *ISPRS Journal of Photogrammetry and Remote Sensing* 64: 117–124. doi:10.1016/j.isprsjprs.2008.09.001.

Mongus, D., N. Lukač, D. Obrul, and B. Žalik. 2013. "Detection of Planar Points for Building Extraction from Lidar Data Based on Differential Morphological and Attribute Profiles." *ISPRS Annals of Photogrammetry, Remote Sensing and Spatial Information Sciences* II-3/W1: 21–26. doi:10.5194/isprsannals-II-3-W1-21-2013.

Mongus, D., N. Lukač, and B. Žalik. 2014. "Ground and Building Extraction from LiDAR Data based on Differential Morphological Profiles and Locally Fitted Surfaces." *ISPRS Journal of Photogrammetry and Remote Sensing* 93: 145–156. doi:10.1016/j.isprsjprs.2013.12.002.

Mongus, D., and B. Žalik. 2012. "Parameter-Free Ground Filtering of LiDAR Data for Automatic DTM Generation." *ISPRS Journal of Photogrammetry and Remote Sensing* 67: 1–12. doi:10.1016/j.isprsjprs.2011.10.002.

Mongus, D., and B. Žalik. 2014. "Computationally Efficient Method for the Generation of a Digital Terrain Model from Airborne LiDAR Data Using Connected Operators." *IEEE Journal of Selected Topics in Applied Earth Observations and Remote Sensing* 7: 340–351. doi:10.1109/JSTARS.2013.2262996.

Morgan, M., and A. Habib. 2002. "Interpolation of LiDAR Data and Automatic Building Extraction." ACSM-ASPRS annual conference proceedings, Washington, DC, April 19–26, 432–441.

Morgan, M., and K. Tempfli. 2000. "Automatic Building Extraction from Airborne Laser Scanning Data." *International Archives of Photogrammetry and Remote Sensing* 33: 616–623.

Naegel, B., and L. Wendling. 2010. "A Document Binarization Method Based on Connected Operators." *Pattern Recognition Letters* 31: 1251–1259. doi:10.1016/j.patrec.2010.04.003.

Najman, L., and M. Couprie. 2006. "Building the Component Tree in Quasi-Linear Time." *IEEE Transactions on Image Processing* 15: 3531–3539. doi:10.1109/TIP.2006.877518.

Niemeyer, J., F. Rottensteiner, and U. Soergel. 2014. "Contextual Classification of LiDAR Data and Building Object Detection in Urban Areas." *ISPRS Journal of Photogrammetry and Remote Sensing* 87: 152–165. doi:10.1016/j.isprsjprs.2013.11.001.

Perret, B., S. Lefevre, C. Collet, and E. Slezak. 2010. "Connected Component Trees for Multivariate Image Processing and Applications in Astronomy." 20th International Conference on Pattern Recognition (ICPR), Istanbul, August 23–26, 4089–4092. IEEE.

Pingel, T. J., K. C. Clarke, and W. A. Mcbride. 2013. "An Improved Simple Morphological Filter for the Terrain Classification of Airborne LIDAR Data." *ISPRS Journal of Photogrammetry and Remote Sensing* 77: 21–30. doi:10.1016/j.isprsjprs.2012.12.002.

Rottensteiner, F., and C. Briese. 2002. "A New Method for Building Extraction in Urban Areas from High-Resolution LiDAR Data." *International Archives of the Photogrammetry, Remote Sensing and Spatial Information Sciences* 34: 295–301.

Rottensteiner, F., and J. Jansa. 2002. "Automatic Extraction of Buildings from LiDAR Data and Aerial Images." *International Archives of the Photogrammetry, Remote Sensing and Spatial Information Sciences* 34: 569–574.

Rottensteiner, F., G. Sohn, M. Gerke, J. D. Wegner, U. Breitkopf, and J. Jung. 2014. "Results of the ISPRS Benchmark on Urban Object Detection and 3D Building Reconstruction." *ISPRS Journal of Photogrammetry and Remote Sensing* 93: 256–271. doi:10.1016/j.isprsjprs.2013.10.004.

Rutzinger, M., F. Rottensteiner, and N. Pfeifer. 2009. "A Comparison of Evaluation Techniques for Building Extraction from Airborne Laser Scanning." *IEEE Journal of Selected Topics in Applied Earth Observations and Remote Sensing* 2 (1): 11–20. doi:10.1109/JSTARS.2009.2012488.

Salembier, P., A. Oliveras, and L. Garrido. 1998. "Antiextensive Connected Operators for Image and Sequence Processing." *IEEE Transactions Image Processing* 2: 176–201.

Salembier, P., and J. Serra. 1995. "Flat Zones Filtering, Connected Operators, and Filters by Reconstruction." *IEEE Transactions on Image Processing* 4: 1153–1160. doi:10.1109/83.403422.

Salembier, P., and M. H. Wilkinson. 2009. "Connected Operators." *IEEE Signal Processing Magazine* 26: 136–157. doi:10.1109/MSP.2009.934154.

Sampath, A., and J. Shan. 2007. "Building Boundary Tracing and Regularization from Airborne LiDAR Point Clouds." *Photogrammetric Engineering & Remote Sensing* 73: 805–812. doi:10.14358/PERS.73.7.805.

Serra, J. 1998. "Connectivity on Complete Lattices." *Journal of Mathematical Imaging and Vision* 9: 231–251. doi:10.1023/A:1008324520475.

Shan, J., and A. Sampath. 2008. "Building Extraction from LiDAR Point Clouds Based on Clustering Techniques." In *Topographic Laser Ranging and Scanning: Principles and Processing*, 423–446. London: CRC Press, Taylor & Francis.

Shao, Y.-C., and L.-C. Chen. 2008. "Automated Searching of Ground Points from Airborne Lidar Data Using a Climbing and Sliding Method." *Photogrammetric Engineering & Remote Sensing* 74: 625–635. doi:10.14358/PERS.74.5.625.

Sithole, G., and G. Vosselman. 2004. "Experimental Comparison of Filter Algorithms for Bare-Earth Extraction from Airborne Laser Scanning Point Clouds." *ISPRS Journal of Photogrammetry and Remote Sensing* 59: 85–101. doi:10.1016/j.isprsjprs.2004.05.004.

Sohn, G., and I. Dowman. 2007. "Data Fusion of High-Resolution Satellite Imagery and LiDAR Data for Automatic Building Extraction." *ISPRS Journal of Photogrammetry and Remote Sensing* 62: 43–63. doi:10.1016/j.isprsjprs.2007.01.001.

Vincent, L. 1993. "Morphological Gray Scale Reconstruction in Image Analysis: Applications and Efficient Algorithms." *IEEE Transactions on Image Processing* 2: 176–201. doi:10.1109/83.217222.

Vosselman, G. 2000. "Slope Based Filtering of Laser Altimetry Data." *International Archives of Photogrammetry and Remote Sensing* 33: 935–942.

Vu, T. T., F. Yamazaki, and M. Matsuoka. 2009. "Multi-Scale Solution for Building Extraction from LiDAR and Image Data." *International Journal of Applied Earth Observation and Geoinformation* 11: 281–289. doi:10.1016/j.jag.2009.03.005.

Wehr, A., and U. Lohr. 1999. "Airborne Laser Scanning—An Introduction and Overview." *ISPRS Journal of Photogrammetry and Remote Sensing* 54: 68–82. doi:10.1016/S0924-2716(99)00011-8.

Wilkinson, M. H. F. 2007. "Attribute-Space Connectivity and Connected Filters." *Image and Vision Computing* 25: 426–435. doi:10.1016/j.imavis.2006.04.015.

Yang, B., W. Xu, and Z. Dong. 2013. "Automated Extraction of Building Outlines from Airborne Laser Scanning Point Clouds." *IEEE Geoscience and Remote Sensing Letters* 10 (6): 1399–1403. doi:10.1109/LGRS.2013.2258887.

Zhang, K. Q., S.-C. Chen, D. Whitman, M.-L. Shyu, J. H. Yan, and C. C. Zhang. 2003. "A Progressive Morphological Filter for Removing Nonground Measurements from Airborne LIDAR Data." *IEEE Transactions on Geoscience and Remote Sensing* 41: 872–882. doi:10.1109/TGRS.2003.810682.

Zhang, K. Q., J. H. Yan, and S.-C. Chen. 2006. "Automatic Construction of Building Footprints from Airborne LiDAR Data." *IEEE Transactions on Geoscience and Remote Sensing* 44: 2523–2533. doi:10.1109/TGRS.2006.874137.

Zhang, Y. J., and X. Shen. 2013. "Direct Georeferencing of Airborne LiDAR Data in National Coordinates." *ISPRS Journal of Photogrammetry and Remote Sensing* 84: 43–51. doi:10.1016/j.isprsjprs.2013.07.003.

Zhao, Z., and A. Saalfeld. 1997. "Linear-Time Sleeve-Fitting Polyline Simplification Algorithms." *Proceedings of AutoCarto* 13: 214–223.